Safer operations in changing ice-covered seas: approaches and perspectives

Book or Report Section

Accepted Version

www.reading.ac.uk/centaur

CentAUR

Central Archive at the University of Reading

Reading's research outputs online

Safer operations in changing ice-covered seas: approaches and perspectives

Yevgeny Aksenov[1], Stefanie Rynders[1], Danny L. Feltham[2]

Lucia Hosekova[2,3], Robert Marsh[4], Nikolaos Skliris[4]

Laurent Bertino[5], Tim D. Williams[5], Ekaterina Popova[1]

Andrew Yool[1], A.J. George Nurser[1] , Andrew Coward[1]

Lucy Bricheno[6], Meric Srokosz[1] and Harrold Heorton[7]

[1] National Oceanography Centre, European Way, Southampton, UK
[2] Centre for Polar Observation and Modelling, Department of Meteorology, University of Reading, Reading, UK
[3] Applied Physics Laboratory, University of Washington, Seattle, WA, USA
[4] School of Ocean and Earth Science, University of Southampton, Southampton, UK
[5] Nansen Environmental and Remote Sensing Centre and Bjerknes Centre for Climate Research, Bergen, Norway
[6] National Oceanography Centre, Joseph Proudman Building, Liverpool, UK
[7] Department of Earth Science, University College London, London, UK.
Contact: yka@noc.ac.uk

Abstract. The last decades witnessed an increase in Arctic offshore operations, partly driven by rising energy needs and partly due to easing of sea ice conditions and improved accessibility of shipping routes. The study examines changes in sea ice and ocean conditions in the Arctic with their implications for off-shore safety. The objective of the research is to develop a basis for forecasting technologies for maritime operations. We assess loads on off-shore structures from sea ice and ocean in centennial climate future projections and implications for the accessibility and future Arctic shipping. As a test case, we calculate loads on a tubular structure of 100-m wide and 20-m tall, similar to installations in the Beaufort Sea in the 1980s. With sea ice retreating, loads are predicted to increase from ~0.1 x 10^6 Newton (MN) at present to ~50–200 MN in the 2090s, primarily

due to wave loads. This study asserts the need for new approaches in forecasting to make marine operations in the Arctic safer.

1. Introduction

The Arctic has become a prominent highlight in climate change news and discussions. Recurrent summer sea ice records apparently support the view that Arctic sea ice is on a long-term decline trajectory, with ice-free summers projected to occur as early as in the 2030s [1]. More evidence from the observational record on the unprecedented changes in the Arctic system has recently come to light, including those in the ocean, sea state, atmosphere, glaciers, subsea permafrost, ocean biology and ecosystems and also on land [2, 3 and 4]. The thinning of the sea ice cover and the appearance of large areas of open water in the summer in the Arctic generate more waves, breaking-up pack ice and creating an area of fragmented sea ice, known as Marginal Ice Zone (MIZ) [5]. This can potentially lead to the further decline of the pack ice and increase of the MIZ area as a proportion of the total ice cover (Figure 1), although the evidence for this from the satellite records remains inconclusive and depends on details of the data processing and the definitions of thresholds.
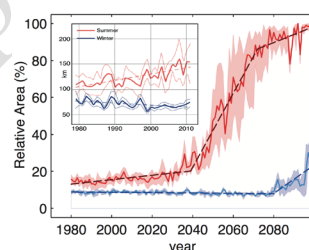
Figure 1. Simulated projected 1980-2100 Marginal Ice Zone (MIZ) relative area [6]. Inset shows MIZ width for 1979-2011 from the satellite data [7]. MIZ is defined as sea ice with fraction of 0.15-0.80. Blue lines are winter MIZ (December–January–February) MIZ and red lines are summer MIZ (June–July–August). The shading and thin lines marks one standard deviation. Dashed lines show fitted linear trends.

Understanding these changes can improve our ability to forecast how the Arctic system is evolving, but can also give us valuable

insights into climate change elsewhere. These new insights will allow us to build more rigorous climate predictions for the next decades to a century. The effects of global warming are translated into a multitude of socio-economics impacts in the Arctic. The last decades have witnessed an increase in Arctic offshore operations, partly driven by increasing energy needs and partly due to easing of sea ice conditions and improved accessibility of the shipping routes [6,8]. A comprehensive assessment of the changes in the environment will allow industries, governing and regulatory bodies and local communities to plan for a variety of economics and societal development scenarios. The study presents an analysis of the environmental risks relevant to future Arctic offshore operations and shipping. The aim is twofold: (i) to examine changes in sea ice and oceanic conditions in the Arctic and (ii) to assess their relevance to off-shore shipping and operations both now and in the future. We use a suite of high-resolution Ocean General Circulation Model (OGCM) simulations to examine key environmental parameters of the current and future climates as far as the end of the century, along with output from the ocean waves model WaveWatch^{TM}III, and apply these to analyse operational risks. The paper is structured as follows: Section 2 introduces analysis methods and describes the OGCM simulations; new environmental variables are presented in Section 3; the present-day climate assessment of structural loads is presented in Section 4; Sections 5 and 6 examine future climate scenarios; Section 7 discusses the results and Section 8 presents summary of the study.

2. Methods

a. Models

For the present-day climate analysis, we use high-resolution global Ocean General Circulation Model (OGCM) NEMO (Nucleus for European Modelling of the Ocean) coupled to Los Alamos sea ice model CICE [9,10]. NEMO is a Boussinesq hydrostatic model and uses finite differences on the global tripolar orthogonal mesh with Arakawa C-grid discretization [11]. To avoid singularity at the North Pole, the mesh has two poles in the Siberia and Canada with the third mesh pole at the South Pole. In the vertical, there are 75 levels with resolution of 1-m at the surface, ~2 m in the top 50 m and ~4 m in the top 100 m. The high model resolution and partial-step model bottom topography improves simulations of the ocean currents on the continental shelf and shelf slope. CICE is dynamics-thermodynamics model, shares the same tripolar mesh but is discretized on Arakawa B-grid.

CICE thermodynamics is energy-conserving, with four layers of ice and one layer of snow to model vertical heat conduction. The balance of the fluxes controls sea ice and snow melting from the top. Surface melt ponds are simulated from a topographic melt pond model. The bottom ice growth and melt are governed by the heat conduction through ice and oceanic heat flux to ice base. Ice age tracer allows to keep track of first-year and multi-year level and ridged ice. The dynamical part of CICE includes continuum Elastic-Viscous-Plastic rheology (EVP), combining non-linear viscous-plastic (VP) rheology with elastic term for regularization of VP for strain rates approaching zero [10]. Sea ice is driven by winds and ocean currents and it resists deformation with a compressive strength that depends on ice thickness and concentration. The momentum balance

accounts for the atmosphere–ice and ice-ocean stresses, Coriolis force, slope of the sea surface and ice internal stresses [10]. The model calculates ice thickness distribution in each model cell from ice thermal evolution and mechanical redistribution; we use five ice thickness categories. Details of the NEMO-CICE and validation are presented elsewhere [11]. NEMO-CICE is employed in forecasting and climate research by the UK Meteorological Office (UKMO), is a part of the Global Monitoring for Environment and Security (Copernicus) and of the Inter-governmental Panel on Climate Change (IPCC) assessments.

For this study we have updated CICE model with collisional rheology to represent fragmented ice dynamics in MIZ [12,13]. To simulate sea ice break-up by waves, floe size distribution (FSD) evolution and wave attenuation by sea ice we developed the Waves-in-ice interaction Module (WIM), based on the framework by Williams et al. [14]. The updates included up-stream scheme for wave advection in sea ice, FSD advection using linear remapping and its evolution following lateral melt of ice floes. We have included wave mixing in the Generic Length Scale (GLS) turbulent closure [13,15]. We have conducted simulations of the coupled NEMO-CICE-WIM at a 1/4° horizontal resolution (28 km globally, 9-14 km in the Arctic) for 1958-2015, forced with 6-hourly atmospheric DRAKKAR reanalysis (DFS5.2) and waves data from the European Center for Medium Range Weather Forecasting (ECMWF) [16]. For the analysis of the future projections output is taken from the NEMO simulations completed by the authors of this study under the *Regional Ocean Acidification Modelling* project (ROAM) forced with the

Representative Concentration Pathway 2.6 and 8.5 (*RCP2.6* and *RCP8.5*) scenarios from IPCC AR5. [3]. These scenarios feature low and high carbon dioxide (CO_2) emissions with moderate and strong climate warming by the end of the 21st century respectively. To examine the future wave field, we use WaveWatch™III spectral wave model (hereafter, WWIII) simulations for the *RCP8.5* scenario completed by the authors under the *Coordinated Ocean Wave Climate Project (COWCLIP)* integrations [17]. The model has the resolution of 0.70°x0.46° in longitudinal and latitudinal directions with a global domain extending from 80°S to 83°N. The simulations were forced with 3-hourly atmospheric 10-m wind and daily sea ice concentration taken from the EC-EARTH model runs. The latter is the 1° NEMO-LIM2 sea-ice-ocean model coupled to 1.125° ECMWF Integrated Forecasting System), integrated for 1970-2100 [18].

b. <u>Model validation</u>

To gain confidence in OGCMs skills to simulate present-day climate we have compared the NEMO-CICE-WIM and NEMO-ROAM simulations with available observations, focusing on sea ice metrics (concentration, thickness and drift) and ocean fields (temperature, salinity, mixed layer depth, sea surface heights and currents). UKMO Hadley Centre Sea Ice and Sea Surface Temperature (HadISST1) and World Ocean Atlas datasets, sea ice thickness from the Pan-Arctic Ice-Ocean Modeling and Assimilation System reanalysis (PIOMAS) and satellite dynamical topography and sea ice drift from CERSAT have been employed [3,6,13]. We concluded that the models are good agreement with observations and fit for the study. Comparison of the future NEMO-ROAM projections with the *Coupled*

Model Intercomparison Project 5 (CMIP5) ensembles shows that NEMO-ROAM sea ice extent, area and concentration fields are very close to the CMIP5 ensemble mean [3,6]. This gives us confidence in the model skills to predict a plausible state of the Arctic sea ice for the CO_2 emissions and climate warming scenarios. The WWIII model has been extensively validated for the open ocean in COWCLIP [18], although, observational uncertainty is still large in ice covered areas [5,19]. We have used technique from the University College London and extracted significant wave heights H_s in MIZ from CryoSat-2 [19]. Comparison of 2002-2015 modelled and observed seasonal averages in the Arctic Ocean and North Atlantic for Winter (December-January-February, henceforth DJF) and Summer (June-July-August, henceforth JJA) shows agreement within 10% for means and standard deviations, giving us confidence in the model simulations (Table 1).

Table 1. Mean significant wave heights H_s(m) and standard deviations for 2002-2015 from model and Cryosat-2 [19].

Region	Arctic (>66°N)	Arctic (>66°N)	Arctic & N.Atlantic >60°N	Arctic & N.Atlantic >60°N	N.Atlantic 60°-66°N	N.Atlantic 60°-66°N
Season	Winter (DJF)	Summer (JJA)	Winter (DJF)	Summer (JJA)	Winter (DJF)	Summer (JJA)
Model H_s(m)	**2.68**±0.79	**1.06**±0.37	**3.02**±0.94	**1.19**±0.46	**3.35**±0.96	**1.31**± 0.46
Cryosat-2 H_s(m)	**2.70**±1.03	**0.97**±0.29	**2.47**±1.21	**1.07**±0.38	**3.04**±1.22	**1.29**±0.46

c. Morison's Equation

Here we describe the use of environmental information to calculate the load maps for the off-shore structures and assess risk for ships. The method follows Morison's equation (henceforth ME) to estimate the total hydrodynamic (waves plus currents) forces. MEis composed of Froude-Krylov force and accelerated fluid force "inertia" terms and a boundary layer influence through the drag term [20,21]. Without

repeating derivation details given in the literature we shall treat the inertia – drag dependent total hydrodynamic load on horizontal cross-section of a thickness dz of a "fixed" cylindrical structure due to ocean waves and spatially and temporarily varying currents as:

$$dF(x, z, t) = \left[\rho A C_M \dot{u} + \frac{\rho}{2} D C_D U |\vec{U}|\right] \cdot dz \tag{1}$$

Here, $\vec{u}(x, z, t)$ and $\dot{u}(x, z, t)$ are the wave-induced velocity and modulus of its time derivative in the location of the structure at a given time t, and $\vec{U} = \vec{U}(x, t)$ is the velocity of the ocean current, assumed to be constant with depth and equal to the ocean surface velocity; x is coordinate in the direction of wave propagation, with $x = 0$ aligned with the vertical axis of the cylindrical structure; z is the vertical coordinate; C_M and C_D are inertia and drag coefficients; $\rho = 1025\ (kg/m^3)$ is seawater density; D is the structure diameter, and $A = \pi D^2/4$ is the cross-section area. For the fixed structures the full derivative of the relative velocity between the structure and the ambient water is neglected in (1). The fixed structure condition can be easily relaxed by adding relative displacement of the structure to this equation, although this is out of the scope of the present study. Here we also neglect the spatial variation in the ambient water flow near the cylinder, assuming undisturbed flow in the immediate vicinity of the cylinder at the scale of the cylinder dimeter D is about the same at any given time. For linear waves propagating in x-direction, wave-induced velocity and acceleration at location $x = 0$ (aligned with the vertical axis of the structure), are given by:

$$u(x = 0, z, t) = \frac{agk}{\omega} \frac{\cosh(k(h + z))}{\cosh(kh)} \cos(\omega t) \tag{2a}$$

$$\dot{u}(x = 0, z, t) = agk \frac{\cosh\big(k(h + z)\big)}{\cosh(kh)} \sin(-\omega t) \qquad (2b)$$

Notations here are as follow: ω is wave angular velocity; a is maximum wave amplitude; k is the wave number; g is acceleration of gravity, h is water column total depth, z is depth, and t is time. The drag term in (1) depends on the velocity, whereas the inertia term depends on the acceleration. Hence, the occurrence of the maximum drag force and the maximum inertia force are lagged by a phase shift of 90° and the maximum force is calculated as the maximum value over a wave period. Both the C_M and C_D are functions of Keulegan-Carpenter number [22,23], a measure for the ratio between the wave height and the cylinder diameter, and Reynolds number (*Re*). In addition, C_D increases with increasing local surface roughness of the structure, whereas C_M decreases with increasing roughness. We use typical values of C_M = 0.3 and C_D = 0.45 [24]. To obtain the total load on the structure F_{tot} we integrate (1) by dz for the whole height of the cylindrical structure. Since the structure displacement is neglected, we can drop the dependency on the coordinate x:

$$F_{tot}(t) = \int_0^Z dF(z, t) \cdot dz \qquad (3)$$

Here, Z is the height of the cylindrical structure. The integration of (3) is done numerically using the Simpson's method. The input variables for the above calculations are as follows. We use the wave peak frequency f_p from the WWIII wave model to calculate angular peak frequency as $\omega = 2\pi f$ and significant wave height H_s to obtain maximum wave amplitude: $a = 1.8 \cdot H_s$. The wave fields from WWIII and ocean currents from NEMO are at hourly frequency. ME in the

above form can be applied to tubular (cylindrical) columns of varying diameters that represents several types of offshore structures typically used in the offshore oil & gas and offshore wind industries: fixed jackets, fixed monopiles, floating (spar type) monopiles and artificial islands. To build a demonstration case, here we use the method for a tubular structure 100-m wide and 20-m tall, the loading changes with diameter, the choice based on structures employed in the North Sea and the Arctic [25].

d. Ice loads

We incorporate forces arising from the ice floes collisions with the structure in the presence of the wave field, considering both frictional and collisional (dynamical) sea ice loads and associating collisional loading with the turbulent velocity of sea ice floes. Using an approach to account for the rapid turbulent velocities of the individual ice floes in sea ice rheology [12,26,27], we split the ice velocity U_{ice} into mean velocity u_{ice} for the model grid cell, area-averaged of all ice floes in the model cell, and a randomly-oriented rapidly fluctuating turbulent velocity u' as: $\vec{U}_{ice} = \vec{u}_{ice} + \vec{u}'$. Following this decomposition, the internal sea ice stress tensor σ is expressed as a sum of the frictional σ_{fr} and collisional σ_{col} parts $\sigma = \sigma_{fr} + \sigma_{col}$, with the sea ice internal force $F_{ice}^{total} = \nabla \cdot \sigma$ being a sum of frictional and collisional forces: $F_{ice}{}^{total} = F_{ice\,frictional} + F_{ice\,collisional}$ [12].

Assuming that a not moving (fixed) structure is imbedded in the drifting sea ice, we adapt the model for sea ice forces on icebergs [28,29] to calculate the frictional loads as:

$$F_{ice\ frictional}(t) = \frac{\rho_{ice}h_{ice}}{2} \cdot D \cdot C_d^{ice} \cdot |\vec{u}_{ice}|^2 \tag{4}$$

Here, $\rho_{ice} = 917(kg/m^3)$ and h_{ice} are the sea ice density and thickness; $\overrightarrow{u_{ice}}$ is ice mean velocity; D is the structure diameter; $C_d^{ice} = 1.0$ is the non-dimensional ice drag coefficient; we chose the highest of the suggested values [28,29,30]. The key feature arising from the structure immobility in Equation (4) is the non-zero load for sea ice moving against the structure for all the non-zero ranges of sea ice concentrations, this renders our calculations of the loads to their maximum values. In contrast, Equation (5) in [28] leads to the same zero loads for the sea ice concentration less than 15 percent (loose ice) or exceeding 90 percent (pack ice), which is not physical and erroneous from the observational data. Hence, the step function applied for sea ice concentration in [28] is not applicable to stationary structures. We note, that our Equation (4) is in the same form as Equation (A2c) given by [29] and this also justifies our approach due to the lack of literature suggesting a better way.

Most of the sea ice models do no calculate turbulent ice velocities, but only mean velocity for a given model time step, this prevents calculating collisional loads, which can be substantial. Using the both mean and turbulent sea ice velocities, we are able to fill this gap and calculate the collisional impact following:

$$\delta F_{ice\ collisional}(t) = h_{ice} \cdot \rho_{ice} \cdot G_t \pi \left(\frac{L_f}{2}\right)^2 \tag{5}$$

with L_f being mean floe size and G_t granular temperature of ice drift, explained below. By definition, the average of the turbulent velocity

u' is zero over a model grid cell, however the associated mass-specific kinetic energy $G_t = {u'}^2/2$, hereafter "granular temperature of ice drift" [12], is not zero. Granular temperature is a model prognostic parameter, calculated from the evolution equation, accounting for sources and sinks in the turbulent ice drift due to air and water turbulence, waves and floe-to-floe collisions [13]. To obtain the total collisional load we need to add collisions of all floes with structure during the given time period. We use "raindrop model" to calculate probability of floes collisions with structures occurring over the model timestep (one hour in our simulations) (see [31] for discussion and further references to the raindrop model). The impact probability of collision of sea ice floe with the structure is given by:

$$P_{collisions}\,(t) = n_o \cdot (L_f + D) \cdot |\overrightarrow{U_{ice}}| \tag{6}$$

In (6) n_0 is the area density of the floes in the model grid cell where the structure is located and is defined as below, where a_{ice} is the ice area in the model cell (with area of a_{cell}) and a_{floe} is the floe area:

$$n_0 = \left(\frac{a_{ice}}{a_{floe}}\right) \cdot \left(\frac{1}{a_{cell}}\right) = \frac{A_{ice}}{(\pi/4 \cdot L_f^2)} \tag{7}$$

The total collisional load on the structure over period ΔT is:

$$F_{ice\;collisional} = \delta F_{ice\;collisional} \cdot P_{collisions} \cdot \frac{\Delta T}{L_f} \tag{8}$$

with $\Delta T = 3600(s)$ being the model time step.

The ice loads calculations require modelling dynamics of the fragmented ice cover and floe collisions. (Simulations of the ice floes dynamics are presented in the next section.) Following the

methodology detailed here, we calculate loads from waves, currents and sea ice using OGCM simulations of the present climate and future projections to compute 2-D spatial maps of the total loads and examine both current hazards in the Arctic environment and changes in the future.

e. Shipping risks

To assess future shipping risks in the Arctic we use approach taken by the Arctic Ice Regime Shipping System (AIRSS) to determine sea ice thickness (age) thresholds for ships of different ice classes being able safely enter and navigate sea ice. AIRSS defines the concept of Ice Numerals (IN) as a sum of Ice Multipliers (IM) for different ice thickness bins $\left[h_{ice}^{i}, h_{ice}^{i+1}\right]$, $i = [1, N]$ weighted by their partial fraction: $IN = \sum_{i=1}^{i=N} A_{it}^{i} \times IM_i$ [6]. IM are obtained empirically for a range of ship classes, the values are given in [6], Table A1. For positive IN, risk from the ice conditions risks is low, ship can sail in sea ice with safe speed assesses from the IN values. If IN is zero or negative, the sailing is unsafe. From IN access maps are being produced.

3. Simulated environmental parameters

To calculate ocean and ice loads on structures the method requires ocean currents, wave heights, ice thickness and fragmentation (floe sizes) and the turbulent velocity of the ice drift [13]. In the MIZ, sea ice cover is broken by ocean waves and consists of mobile ice floes. Sea ice drift in the MIZ is subject to large variations due to wind and water turbulence, wave surge and internal ice stresses which are transmitted through floe-to-floe collisions [13]. Here we analyse the NEMO-CICE-WIM simulations 2000-09. The results show that sea

ice presence rapidly attenuates wave energy within ~50–100 km distance of the ice edge. In the ice-free regions of the Norwegian, Greenland and Barents seas, wave height can reach 3 m in winter.

In summer ice floes sizes can decrease to <200 m in the Arctic Ocean and the seasonal ice retreat opens Arctic shelf seas to waves up to 2-m high (Figure 2). The inner boundary of the summer MIZ (defined as an ice fraction of 0.80 [7]) moves northward, beyond the continental shelf slope, and the southern periphery of the pack ice is transformed into MIZ (Figure 2). Seasonally, floe sizes in the MIZ increase in mode values from 20–30 m in winter to 30–40 m in summer due to the melting of the small ice floes (Figure 3).
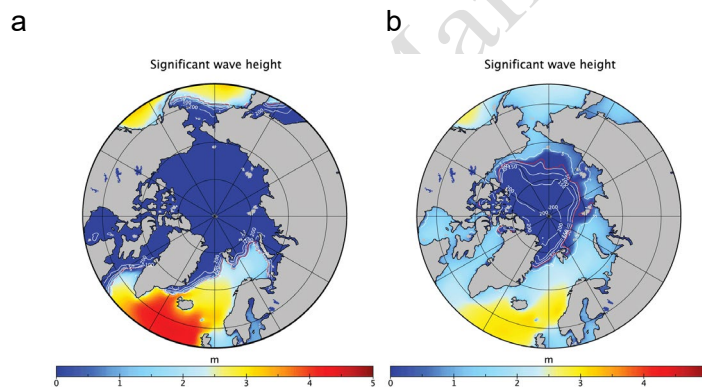

Figure 2. Winter (DJF) (a) and summer (JJA) (b) 2000-2009 seasonal variations in wave heights (colour), with floe sizes (white contours). Magenta marks MIZ inner boundary (0.8 ice fraction). NEMO-CICE-WIM simulations.
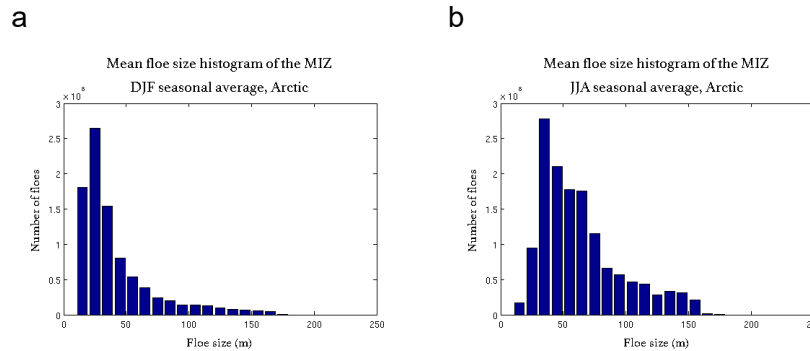
a

b

Figure 3. Floe size distribution in the Arctic Marginal Ice Zone (MIZ) in winter (a) and summer (b) 2000—2009 from NEMO-CICE-WIM simulations.
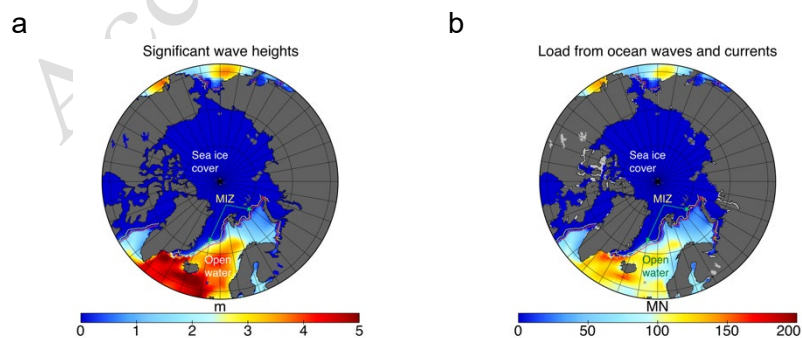
4. Loads on off-shore structures

To estimate present-day loads on off-shore structures, and the associated risks, we calculate combined loads from the ocean (waves and currents) and frictional and collisional loads from sea ice as set out in Section 2.

We choose January 2014 as a typical winter period with a strong storm in the North Atlantic and extensive Arctic ice cover to assess relative contributions from different environmental factors in these conditions. The analysis can be easily extended to synoptic and seasonal scales; however, this is beyond the scope of this study.

In the ice-free North Atlantic, the ME model predicts that wave loads reach 50–200 x 10^6 Newton (MN) and dominate the total load. Here the waves are 4–5 m in height and peak loading maps well onto the areas with maximum wave heights (Figure 4a,b – open water and ice covered areas are marked). In the ice-covered Arctic Ocean the contribution to the total load from the waves and currents are substantial, at 60–80% in some areas (Figure 4c), although the

overall loads from waves, current and sea ice are of *o(0.10 MN)*, much smaller than in the open ocean. Ice loads are of the same magnitude as the wave loads and the spatial distribution of the ice load complements that of the wave load, with the ice load fraction increasing up to 80% in the areas of ice convergence on the Laptev, East-Siberian, Chukchi and Beaufort seas (cf. Figure 4c,d). The ice loads in the central Arctic Ocean result almost entirely from frictional loading, with the collisional load of contributing up to 60–90% of the total load in MIZ in the Icelandic, Greenland and Bering seas, in the Baffin Bay and Hudson Bay and in the Laptev and Beaufort seas due to the high turbulent energy of ice motion (granular temperature) (Figures 4d and 5a). Spatial variability of the collisional ice load is influenced by variation in the floe sizes (mass factor) and granular temperature of ice. Floe sizes decrease in the MIZ towards the ice edge due to break-up, with ice granular temperature higher in the MIZ (Figures 2 and 5a). As a result of these two competing tendencies, the area of the maximum ice collisional loads in the MIZ coincides with areas with a sea ice fraction of ~0.15-0.80 (a band of the higher ice load between the red and yellow lines in Figure 4d).

a
Significant wave heights

b
Load from ocean waves and currents

c — Contribution from ocean waves and currents
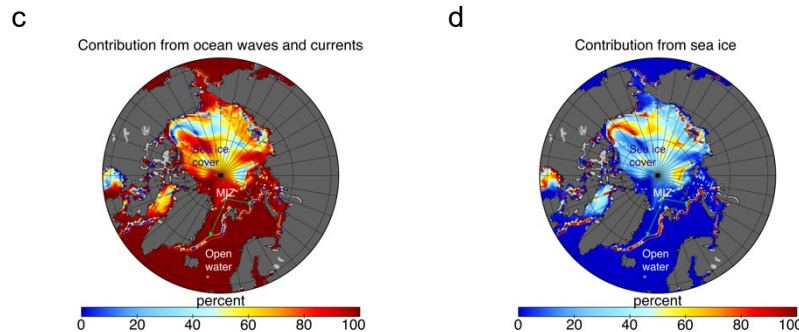
d — Contribution from sea ice

Figure 4. Significant wave height (a) and loads on structures from waves and currents in January 2014 (b). (c) and (d) show the contributions of waves and currents and of sea ice to the total loads. Red and yellow lines mark MIZ boundaries. NEMO-CICE-WIM simulation.

It should be noted that the load contributions from different factors vary substantially on the synoptic scale (5–7 days), with wave and ice loads increasing during storm events. During the storm in January 2014, the collisional loads on the virtual structure in the Greenland Sea increased about 100-fold (to 0.4 MN) on the 22 January 2014 and then a further 2-fold (to ~0.7 MN) on the 30 January 2014 (Figure 5a,b). The contribution of the ocean currents to the loads is more moderate. Average values in the Arctic Ocean are of *o(0.01 MN)*, with the loads peaking at of ~0.08–0.20 MN where there are strong surface currents. For example, in the Bering Strait inflow; north of Barrow; off the Norwegian coast; in the East and West Greenland current systems; and east of Baffin Island and Labrador (not shown).

5. Future changes in the ocean and sea ice

Arctic sea ice decline in all seasons during the last four decades has been documented in satellite data and OGCMs with a variable but overall reasonable degree of robustness [1,18]. Future projections of the Arctic marine environment present scenarios for sea ice changes,

although changes in the ocean are not often examined in detail [6]. Here we combining outputs from the OGCM and WWIII simulation [3,17] and use these in Section 6 to assess projected loads on off-shore structures and risks for shipping.

a

June 2009

m2/s2

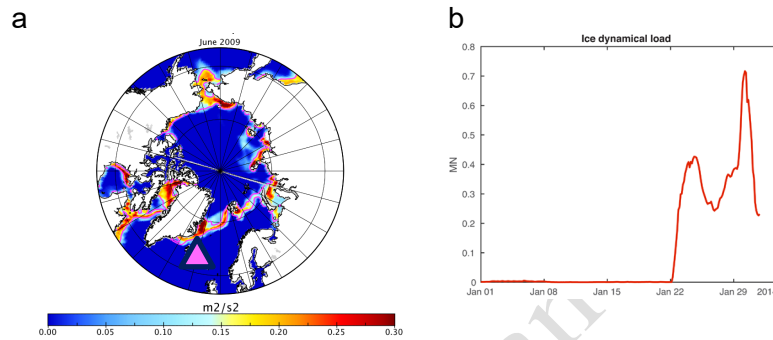0.00 0.05 0.10 0.15 0.20 0.25 0.30

b

Ice dynamical load

Figure 5. (a) Sea ice granular temperature in NEMO-CICE-WIM in January 2014. (b) Ice collisional (dynamical) load on a virtual structure on the Greenland Shelf, location marked with the magenta triangle in (a). Magenta shows MIZ boundaries.

The most striking result of the forward OGCM simulations is the extension of the ice-free season later into the year, leaving Arctic virtually ice-free until December in the 2090s (Figure 6a). Following the open ocean conditions, Figure 6 shows development of strong storms with waves reaching in excess of 5 m in the Norwegian and Beaufort seas (maximum wave height reaches 9 m off the Norwegian coast). These are analogues of the 2012 storm [5], but with stronger wind and waves. The lower ice conditions increase momentum transfer to the ocean from the atmosphere, accelerating spin-up of the ocean currents and faster drift of the fragmented sea ice (Figure 6b,d). This drift can form "ice jets" [13] with a large spatial shear in ice deformations in the Beaufort Sea, on the North and East

Greenland continental shelves, in the Canadian Archipelago and Baffin Bay. (Figure 6b). Significantly, these areas are mineral-rich and are considered prospective for off-shore mining. The patterns of ocean currents also change in these simulations, with the Fram Strait branch of the Atlantic inflow diminishing, and an accelerated Arctic Boundary Current along the Siberian shelf slope (Figure 6d). The Beaufort Gyre has been predicted to shift from its current position in the west Beaufort Sea to the shallow Chukchi Cap, spinning-up strong eddies off-shore, and affecting ocean currents in the immediate vicinity of the shallows and in the Canada Basin (Figure 6d). The westward shift of the Beaufort Gyre has already been recorded in satellite data, showing agreement between the observations and models. In conclusion, the sea ice retreat significantly affects upper ocean dynamics and sea state (waves). These changes are expected to impact future environmental extremes and to affect hazards ranking for marine operations discussed in the next sections.

6. Risks and loads in the future projections

We used model output from the forward high-resolution forced centennial (2000-2099) simulations described previously [3], and analysed low (*RCP2.6*) and high (*RCP8.5*) emission scenarios to estimate future projected global loads from sea ice and ocean currents using the methodology described in Section 2. Since it is computationally expensive to run fully-coupled wave-sea ice-ocean models, we used a stand-alone WWIII wave model forced with projected atmospheric model output (to 2099) [17,18] to obtain an estimate of the wave loads in the future scenarios. Note that this

approach is limited by its omission of wave-ocean feedbacks. To the best of the authors' knowledge there are only few analyses published on the projected wave climate in the Arctic, and these do not take sea ice-waves-ocean interaction processes into account either [32].

The results find that wave loads dominate the total forces experienced by structures with magnitudes of *o(100MN)* in the high emission scenario *RCP8.5* (Figure 7a). In these simulation total loads from waves reach very high values during the storm events in the Norwegian Seas and also in the most of the Arctic Ocean (Figure 7a)*.* In the *RCP8.5* simulations Arctic summer sea ice disappears by 2060s [6]. By 2090, winter sea ice is largely absent in the Arctic Ocean except for thin ice on the Siberian shelves (0.2 m) and the Canadian Archipelago (0.6 m). Total ice loads in the high scenarios become negligible by the mid 21-st century due to low ice cover*.* However, in the 2030s, ice loads are still the second highest, of *o(10MN)* (Figure 7b).
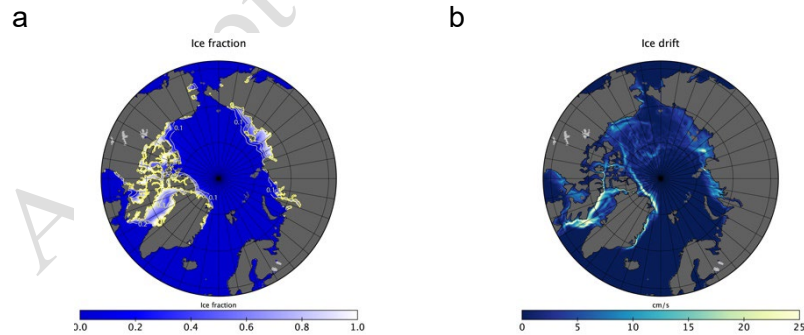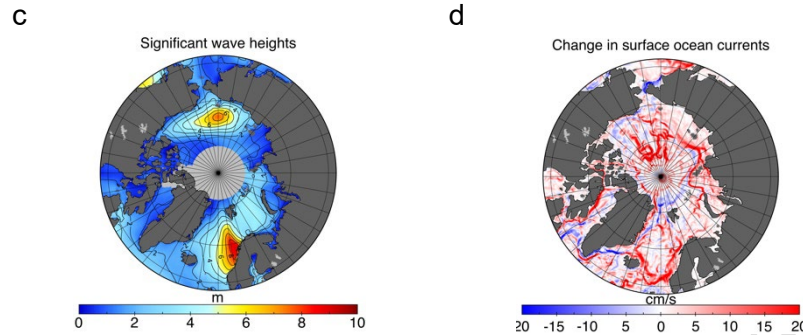
Figure 6. Future Arctic in Jan 2090 (*RCP8.5*): (a) sea ice fraction (colour) and thickness (contours); (b) ice drift and (c) wave heights; (d) surface currents change 1990s to 2090s. (a,b,d) – from the high-resolution forward NEMO-ROAM simulations; (c) – WWIII. The light grey shading around the North Pole in (c) shows area outside WWIII model domain.

Total loads from ocean currents are lower still, order of *o(0.1MN),* in both low and high scenarios (results not shown). Meanwhile, in the *RCP2.6* simulations total ice loads remain significant until the end of the century, contributing of 10-15% to the total total loads in the 2030s in the Central Arctic Ocean and up to 70-100% of total forces (results not shown). Sporadic high ice loading (reaching up to 100% of total loads) can also occur in the both emission scenarios in the mid-century in areas of ice drift convergence – the Arctic Transpolar Drift and north of Greenland. These are primarily from loading due to floe collisions with structures.
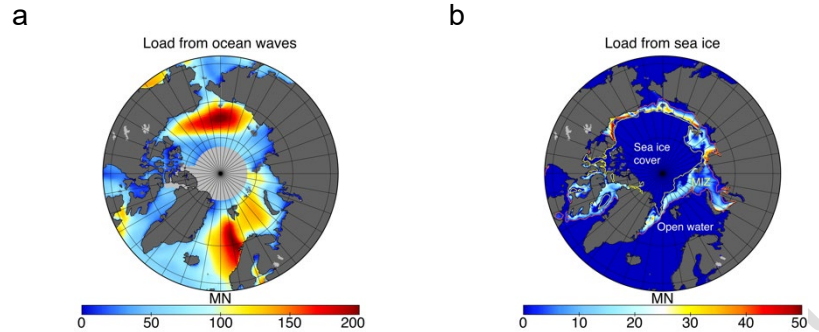
a
Load from ocean waves

b
Load from sea ice

Figure 7. Wave loads on virtual structure in mid-January 2090 calculated from WWIII run with *RCP8.5* forcing (a) and total sea ice load in July 2030-39 in the same *RCP8.5* scenario from the NEMO-ROAM simulations (b). The light grey shading around the North Pole in (a) shows area outside WWIII domain. Red and yellow lines in (a) mark outer and inner MIZ boundaries (0.15 and 0.80 of ice fraction).

Using accessibility maps based on AIRSS (Arctic Ice Regime Shipping System) model [6] we compared high-load risk areas from different environmental factors to illustrate regional differences for the marine operational hazards. From the *RCP2.6* forward simulations we have assessed accessibility in summer (JJA) 2030-39. The accessibility analysis has been based on the safe speed criteria for ship classes Type B and CAC4 [6] and the accessibility has been presented as a "traffic light" factor based on the Ice Numerals method [6]. Figure 8 shows accessible areas in green (Ice Numeral > 0, safe to sail in) and inaccessible areas in red (Ice Numeral <= 0, not safe to sail in) for the two ship classes, general cargo Type B vessel and CAC4 ice-capable vessel, for the projected average summer (JJA) sea ice conditions in 2030-39 from the *RCP2.6* high-resolution forward simulations. In this decade the projected summer sea ice extent is similar to the present day, with the ice fraction is about 0.8-1.0, however ice is thinner, only ~0.5-1.5 m thick in the central Artic Ocean and less than 0.5-m thick in the

Siberian shelf seas. These allows CAC4-type ice-capable vessels to sail unsupported by North Sea Route (NSR), whereas Type B general vessels cannot access the NSR without ice-breaker support. This analysis is in agreement with the Arctic navigability assessment from [6], although the approach taken by AIRSS includes only "static" risks from sea ice, aka areas covered by heavy ice, neither addresses risks from ice convergences nor from ice floes collisions with ship hull nor in calm seas nor in wavy conditions.
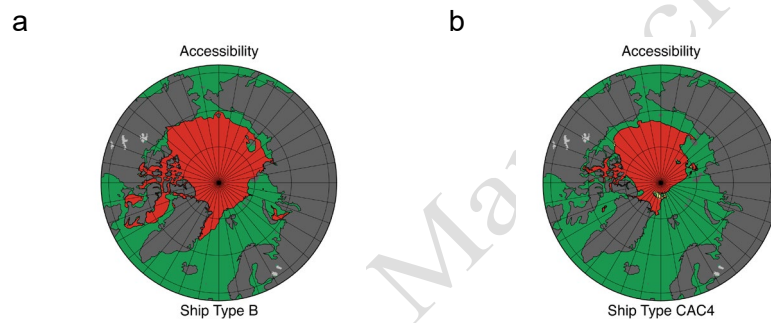
a   b

Figure 8. Risk areas as "traffic lights". (a,b) accessibility based on AIRSS model [6] in summer (June-July-August) 2030-39 for ship classes Type B and CAC4; *RCP2.6* forward NEMO-ROAM simulations.

Comparison of the ship accessible areas in Figure 8 with areas of the high ice loads in Figure 7b demonstrates that the standard accessibility models can be underestimating the ice loads and risks in MIZ. The higher wave loads alos broadly correspond to the areas of the higher ice loads in MIZ. Where sea ice is broken and piling up against the coast, the collisional loads are high in the presence of the high wave loads, e.g. the areas around the islands and north of the Cape Barrow, increasing combined risk from waves and ice dynamics. Keeping in mind that the time periods for the waves loads and ship accessibility analysis are for winter *vs*. summer, the overall

conclusion is clear: the areas for the risks from waves are mostly on the Siberian shelf, whereas higher ice hazards are in the central Arctic Ocean, where there is more ice and less waves.

7. Discussion

In the analysis presented here, loads on Arctic structures are predicted to increase from ~0.1 MN at present to ~50–200 MN in the future, primarily due to increased wave loads. Although Arctic sea ice is simulated to decline into the future, ice loads will also increase due to dynamical impacts from floe-structure collisions, but remain of secondary importance at ~20-50 MN (cf. Figures 4 and 7). These results challenge the view that the risks for off-shore operation in the Arctic will diminish with sea ice reduction [8]. Our analysis also predicts loads from ocean currents to increase from the present peak level of ~0.01 MN to ~0.3 MN in the central Arctic in the future projections due to the acceleration of ocean currents, whereas frictional ice load decreasing from with reduced ice fraction and thickness.

The ME method used in the study has several limitations that can affect its results. The presented analysis focuses on mono-piles with large width. Since the inertia term in the Equation (1) depends on D^2 and the drag term depends linearly on D , the width of the structure is more important for wave loads (as they quickly attenuate with water depth), whereas the structure height is more important for current loads. Consequently, different dimensions and types of structure will experience different loads. It is possible to scale the load for the tubular structures of various diameters and the analysis can be extended to the structures of various heights and a number of jacket legs. We have performed such an analysis for the fixed 100-m tall

monopiles with diameters 1m-10m in the Northern Sea [25]. The results demonstrated that the wave force is at least an order of magnitude larger (~50 MN for 10-m diameter structure) than the current force. Relatively large current contribution is in the tidally-dominated areas (~1 MN for 10-m diameter structures) or in deeper regions, whereas large wave force is in shallow water. Our analysis excludes tides, these are important in the North Sea. In the Arctic tides may be crucial in regions, such as the Sea of Okhotsk.

Higher ice thickness in the ridges and higher strength of the consolidated ridges can result in higher loads. We used averaged ice velocities, in reality there is a fast stick-sleep loading of the structures. The above assumptions may explain lower ice frictional loads in our analysis as compared to the measured local loads on off-shore structures in the Arctic [25,33]. As a next step we plan to use the ice strength from the model to calculate deformation scale of the ice floes. This would allow to detect the different regimes of the floe-structure collision.

While our work has used what are currently high resolution models, even higher resolutions (<1 km) will further increase the speed of simulated currents and the resulting loads from them. Similarly, higher resolution will result in faster sea ice drift and higher ice stresses, making ice loads larger [34]. Collisional ice loads have a strong sensitivity to ice floe sizes due to their dependency on floe mass: in our calculations the loads in-crease ~100-fold when mean floe size increases from 50m to 300m. However, for ice–ship interactions, the AIRRS model does not include collisions with ice floes, underestimating risks. Linking floe sizes with their dynamical impact on ship hulls from scaled model ship basin experiments and

Discrete Element Modelling (DEM) provides method of assessment [35]. The environmental models used in this study do predict iceberg trajectories and their probabilistic distribution and risk of collision [11]. However, to estimate the loads and damage due to ship-icebergs collision the full external and internal mechanics should be considered [36]; this requires additional development linking the environmental modelling with ship mechanics. The above uncertainties are likely to result in the underestimation of loads and associated risks for other factors than sea ice, therefore supporting the main conclusion of the study that future sea ice retreat, while opening the Arctic to off-shore industries, may lead to higher risks from emerging environmental factors.

8. Summary

The reduction of the Arctic sea ice cover in the last decades has led to the easing of conditions for summer navigation along the NSR and an episodic opening of the Northwest Passage Route (NWP). This is often interpreted as overall improvement of marine access in the Arctic. However, the combined changes in sea ice cover and the ocean are not addressed in these assessments. In this study we have examined environmental factors which may increase risks to marine operations in the future. These environmental parameters should be considered in marine accessibility and risks planning for off-shore structures and navigation. The emerging future Arctic features more fragmented and active sea ice, as well as a more active ocean. These changes in the environment consequently require new approaches in monitoring and forecasting of the ocean and sea ice. New fundamental developments are also important for constraining future projections and improving forecasting skills, ultimately making

navigation and off-shore marine industries in the Arctic safer for the environment and society.

References
[1] Stroeve et al. (2012). Trends in Arctic, Geophys. Res. Lett., 39, L16502.
[2] Polyakov et al. (2017). Greater role for Atlantic, Science 356(6335).
[3] Yool et al. (2015). Future change in ocean productivity. J. G. Res. 120(12).
[4] Shakhova et al. (2017). Current rates permafrost Nat.comm.8, 15872.
[5] Stopa et al. (2016). Wave climate in the Arctic. Cryosph. 10(4).
[6] Aksenov et al. (2017). On the future navigability, M.Pol.75, 300-317.
[7] Strong & Rigor (2013). Arctic marginal ice zone. Geophys. Res. Lett. 40(18).
[8] Melia et al. (2016). Sea ice decline, Geophys.Res.Lett 43, 9720–9728.
[9] Madec G. (2014). "NEMO ocean engine". IPSL, France, No 27 ISSN 1288–1619.
[10] Hunke et al. (2013). CICE, Los Alamos Nat. Lab., NM 87545.
[11] Storkey et al. (2018). UK Global Ocean GO6 and GO7. Geosci. Mod. Dev. 11(8).
[12] Feltham (2005). Granular flow ... Phil.Trans.R.Soc. 363, 1677–1700.
[13] Rynders et al. (2020), Impact of granular behaviour of fragmented…, this issue.
[14] Williams et al (2013). Wave–ice interactions in the marginal... Oc. Mod., 71.
[15] Bateson et al. (2019). Impact of floe size distribution, Cryosph. 1–35.
[16] Brodeau et al. (2010). An ERA40-based atmospheric forcing. Oc. Mod. 31.
[17] Bricheno & Wolf (2018). Future wave conditions. J.Geophys.Res. 123.

[18] Morim et al. (2020). A global ensemble of ocean wave climate... Sci. Data 7(1).
[19] Heorton et al. (2020). Remote. Sens. submitted.
[20] Morison et al. (1950). The force exerted by surface …. Petr. Trans. AIME 189.
[21] Chakrabarti (1987) Hydrodynamics of Offshore Structures. Springer Verlag.
[22] Keulegan & Carpenter (1958). Forces on cylinders. J.Res.Nat.Bur.Stand. 60(5).
[23] Clauss et al. (1992). Hydromechanical Analysis of Offshore... Springer, London.
[24] Halse (1997). On vortex shedding …. Norwegian University of Sci. Tech..
[25] Sanderson (1988). Ice Mechanics; Risks to offshore structures, Boston.
[26] Haff (1983) Grain flow as a fluid-mechanical phen. J. Fluid Mech. 134, 401–430.
[27] Shen et al. (1987). The role of floe collisions. J. Geophys. Res. 92, 7085–7096.
[28] Lichey & Hellmer (2001). Modeling giant-iceberg drift. J.Glac. 47(158), 452-460.
[29] Martin & Adcroft (2010). Parameterizing the fresh. Oc. Mod. 34(3-4), 111-124.
[30] Timco& Weeks (2010). A review of the engineering. Cold Reg. Sci. Techn 60(2).
[31] Onishchenko (2009). Analytical approach to the calculation (No. POAC09-126).
[32] Khon et a. (2014). Wave heights in the 21st cent. Geophys. Res. Lett. 41(8).
[33] Jefferies et al (2011). Ice load measurement on Molikpaq: (No. POAC11-189).
[34] Lemieux et al. (2020). Toward a method for downscaling. Cryosp.14,3465-3478.
[35] Huang et al. (2019). Simulation of a ship advancing in floating ice floes (POAC).
[36] Liu & Amdahl (2010). A new formulation of the impact... Marine Struct., 3(23).